

Article

Optimization of Curvi-Linear Tracing Applied to Solar Physics and Biophysics

Markus J. Aschwanden ^{1*}, Bart De Pontieu ¹, and Eugene A. Katrukha ²

¹ Lockheed Martin Solar and Astrophysics Laboratory, Bldg. 252, Org. A021S, 3251 Hanover St., Palo Alto, CA 94304, USA

² Cell Biology, Faculty of Science, Utrecht University, Padualaan 8, 3584CH, The Netherlands

* Author to whom correspondence should be addressed; aschwanden@lmsal.com, Phone: 650-424-4001, Fax: 650-424-3994.

Version November 10, 2021 submitted to *Entropy*. Typeset by \LaTeX using class file *mdpi.cls*

Abstract: We developed an automated pattern recognition code that is particularly well suited to extract one-dimensional curvi-linear features from two-dimensional digital images. A former version of this *Oriented Coronal CURved Loop Tracing (OCCULT)* code was applied to spacecraft images of magnetic loops in the solar corona, recorded with the NASA spacecraft *Transition Region And Coronal Explorer (TRACE)* in extreme ultra-violet wavelengths. Here we apply an advanced version of this code (*OCCULT-2*) also to similar images from the *Solar Dynamics Observatory (SDO)*, to chromospheric H- α images obtained with the *Swedish Solar Telescope (SST)*, and to microscopy images of microtubule filaments in live cells in biophysics. We provide a full analytical description of the code, optimize the control parameters, and compare the automated tracing with visual/manual methods. The traced structures differ by up to 16 orders of magnitude in size, which demonstrates the universality of the tracing algorithm.

Keywords: Solar physics; magnetic fields; biophysics; automated pattern recognition methods

1. Introduction

Image segmentation is an image processing method that subdivides an image into its constituent regions or objects, which can have the one-dimensional geometry of curvi-linear (1D) segments, or the two-dimensional (2D) geometry of (fractal) areas. Common techniques include point, line, and

19 edge detection, edge linking and boundary detection, Hough transform, thresholding, region-based
 20 segmentation, morphological watersheds, etc. (e.g., [14]). Since there exists no omni-potent automated
 21 pattern recognition code that works for all types of images equally well, we have to customize suitable
 22 algorithms for each data type individually by taking advantage of the particular geometry of the
 23 features of interest, using *a priori* information from the data. In this study we optimize an automated
 24 pattern recognition code to extract magnetized loops from images of the solar corona with the aim of
 25 optimum completeness and fidelity. We will demonstrate that the same code works also equally well
 26 for microscopic images in biophysics. The particular geometric property of the extracted features is
 27 the relatively large curvature radius of coronal magnetic field lines, which generally do not have sharp
 28 kinks and corners, but exhibit continuity in the variation of the local curvature radius along their length.
 29 Using a related strategy of curvature constraints, coronal loops were extracted also with the directional
 30 2D Morlet wavelet transform ([7]). In addition, solar coronal loops, as well as biological microtubule
 31 filaments, have a relatively small cross-section compared with their length, so that they can be treated as
 32 curvi-linear 1D objects in a tracing method. Tracing of 1D structures with large curvature radii simplifies
 33 an automated algorithm enormously, compared with segmentation of 2D regions with arbitrary geometry
 34 and possibly fractal fine structure [22].

35 The content of this paper includes a brief description of the automated tracing code (Section 2),
 36 applications to images in solar physics (Section 3), to images in biophysics (Section 4), discussion and
 37 conclusions (Section 5), and a full analytical description of the code in Appendix A.

38 2. Description of the Automated Tracing Code

39 Early versions of *Oriented-Connectivity Methods (OCM)* applied to solar images were pioneered by
 40 Lee, Newman, and Gary [18,19]. This code was applied to a *Transition Region And Coronal Explorer*
 41 (*TRACE*) image and a total of 57 coronal loops were detected in a solar active region, which supposedly
 42 outline the dipolar magnetic field. The results of this code were compared among five numerical codes
 43 based on similar curvi-linear loop-segmentation methods in a study of Aschwanden [3], in terms of
 44 the cumulative size distribution of loop lengths, the median and maximum detected loop lengths, the
 45 completeness and detection efficiency, accuracy, and flux sensitivity. One of these codes was developed
 46 further, which we call *Oriented Coronal CURved Loop Tracing (OCCULT)* code, and was found to
 47 approach the quality of visually and manually traced loops, detecting a total of 272 loop structures in
 48 the same TRACE image [4]. In the study here we developed this code further and tested it in a larger
 49 parameter space and with different types of images. Technical details of the original OCCULT code are
 50 given in [4], a concise description of the advanced OCCULT-2 code is given in the following, while a
 51 comprehensive analytical description of OCCULT-2 is provided in Appendix A.

52 1. **Background supression:** The median z_{med} of an intensity image $z_{ij} = I_0(x_i, y_i)$ is computed, and
 53 the low intensity values with $z_{ij} < z_{min}$ are set to the base value $z_{min} = z_{med} \times q_{med}$, with q_{med}
 54 being a selectable control parameter, with a default value $q_{med} = 1.0$ if applied, and $q_{med} = 0$ if
 55 ignored, while a range of $1 \lesssim q_{med} \lesssim 2.5$ was found to be useful for noisy data. The median value
 56 z_{med} is a good estimate of the background (if the features of interest cover less than 50% of the
 57 image area) and can manually be adjusted with the multiplier q_{med} otherwise. The parts of the

original image that have intensities below this base level, are then rendered with a constant value, are noise-free, and will automatically suppress any structure detection in the background below this base level. This new method is more flexible and efficient in suppressing faint background structures.

2. **Highpass and lowpass filtering:** A lowpass filter with a boxcar smoothing constant n_{sm1} smoothes out the data noise (e.g., photon noise with Poisson statistics in astrophysical and microscopy images, e.g., see [24]), while a highpass filter with a boxcar smoothing constant n_{sm2} enhances the fine structure. The two combined filters represent a bandpass filter (with $n_{sm1} < n_{sm2}$), defined by

$$I^{filter}(x_i, y_j) = smooth[I_0(x_i, y_j), n_{sm1}] - smooth[I_0(x_i, y_j), n_{sm2}]. \quad (1)$$

For theoretical and experimental reasons, a filter combination of $n_{sm2} = n_{sm1} + 2$ yields the sharpest enhancement of the intermediate spatial scale, and thus warrants optimum performance in tracing of curvi-linear structures.

3. **Initialization of loop structures:** The code initializes the first structure to be traced from the position (x_0^a, y_0^a) with the maximum brightness or flux intensity $f_0^a = I_0(x_0^a, y_0^a)$ in the original image $I_0(x, y)$. Once the full loop has been traced, the area of the detected loop is erased to zero, and the next loop structure is initialized at the position (x_0^b, y_0^b) with the next flux maximum f_0^b in the residual image. The initialization of subsequent loops (f_0^c, f_0^d, \dots) is continued iteratively until the residual image becomes entirely zeroed out, the increase of detected structures stagnates, or a maximum loop number N_{max} is reached.
4. **Loop structure tracing:** An initialized structure starting at its flux maximum position (x_0, y_0) is then traced in forward direction to the first end point of the loop, and then in opposite direction from the original starting point to the second endpoint. The two bi-directional segments are then combined into a single uni-directional 1D path $s_i = s(x_i, y_i), i = 1, \dots, n_s$. The step-wise tracing along a loop structure position s_i is carried out by determining first the direction of the local ridge (defined by the azimuthal angle α_l with respect to the x -axis), and secondly by determining the local curvature radius r_m . The curved segment that follows a local ridge closest, is used as a second-order polynomial to extrapolate the traced loop segment by one incremental step (of $\Delta s = 1$ pixel). This second-order guiding criterion represents an improvement over the first-order guiding criterion used in the previous OCCULT code [4]. The second-order guiding criterion is defined by the brightness distribution $f(s) = f[x_{seg}(s), y_{seg}(s)]$ along a loop segment with constant curvature radius and length n_s . If the segment follows an ideal ridge with a constant curvature radius and a constant brightness, the summed (or averaged) flux along the ridge segment has a maximum value, while it exhibits a minimum in perpendicular direction to the ridge, where the brightness profile collapses to a δ -function.
5. **Loop subtraction in residual image:** Once a full loop structure has been traced, the loop area $I_0(x_i \pm w, y_j \pm w), i = 1, \dots, n_s$, is set to zero within a half width of $w = (n_{sm2}/2 - 1)$, so that the area of a former detected loop is not used in the detection of subsequent loops. However, crossing loops can still be connected over a gap.

91 The original automated loop tracing code (OCCULT) employed the following control parameters:
 92 the highpass filter boxcar n_{sm2} , the noise threshold level N_σ , the minimum curvature radius r_{min} , the
 93 moving segment length n_s , the directional angle range $\Delta\alpha$, and a filling factor q_{fill} for the guiding
 94 criterion. In the advanced code (OCCULT-2) we use only two free parameters: the lowpass filter n_{sm1} ,
 95 and the minimum curvature radius r_{min} . In addition, noise treatment is handled by selecting a typical
 96 noise area in the image, as well as the control factor q_{med} that ignores faint structures below the base level
 97 $z_{min} = z_{med} \times q_{med}$. Thus, the new version of the code offers a simpler choice of control parameters for
 98 automated detection of structures.

99 3. Application to Solar Physics

100 In the following three subsections we process three different types of solar images, one from the
 101 TRACE spacecraft (Section 3.1), one from the SDO spacecraft (Section 3.2), and one from a ground-
 102 based solar telescope (Section 3.3). Some parameters of the analyzed images are listed in Table 1.

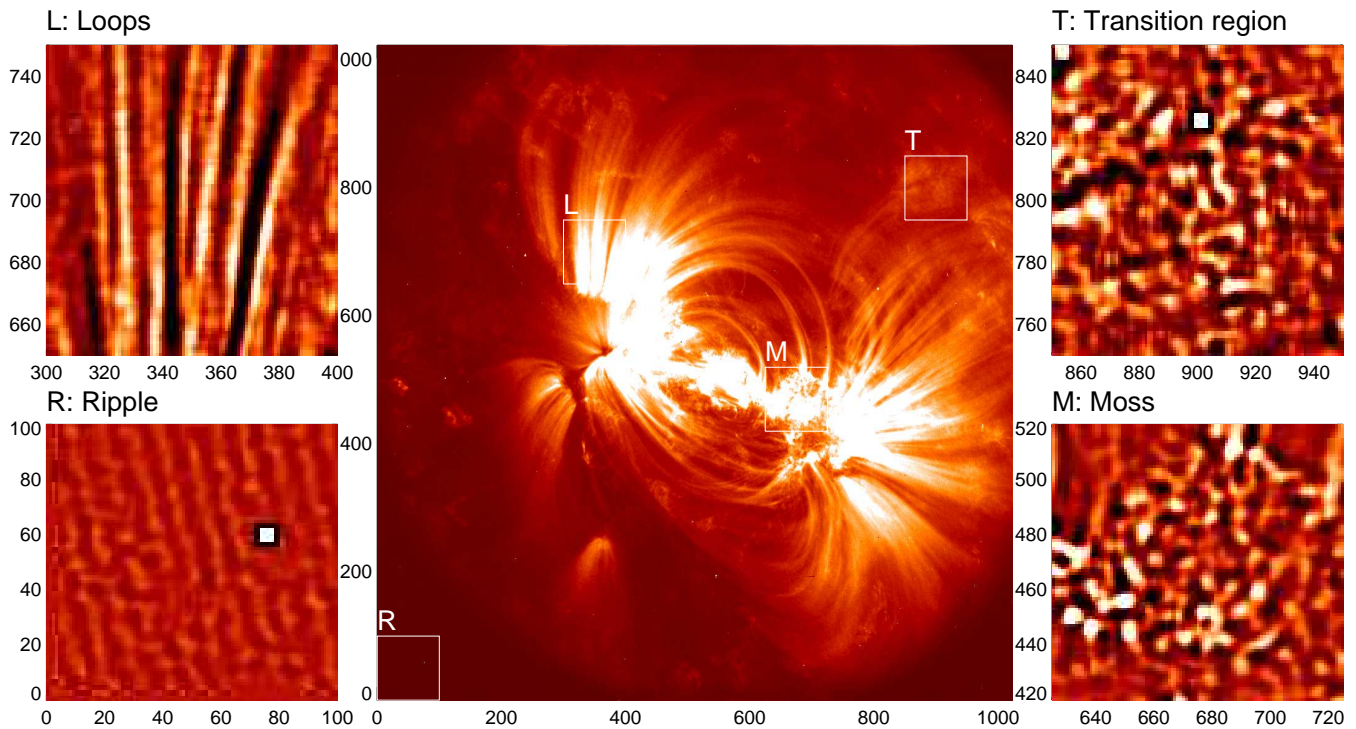
Table 1. Parameters of five analyzed images, including the range of brightness in the image (z_{min}, z_{max}), the minimum curvature radius r_{min} (in units of pixels), the bandpass filter (n_{sm1}, n_{sm2}), the total number of detected loops $N_{det}(L > 30)$, the number of detected long loops $N_{det}(L > 70)$, and the powerlaw slope of the cumulative length distribution p_L .

Image	Brightness range z_{min}, z_{max}	Minimum curvature r_{min}	Filter range n_{sm1}, n_{sm2}	Number of all loops $N_{det}(L > 30)$	Number of long loops $N_{det}(L > 70)$	Powerlaw slope p_L
TRACE	56, 2606	30	5, 7	437	134	3.1
SDO/AIA	28, 255	30	9, 11	503	121	2.7
SST	339, 916	30	3, 5	1757	376	3.9
Cell-HC	416, 65535	15	3, 5	208	51	3.1
Cell-LC	289, 18699	30	7, 9	151	39	2.7

103 3.1. TRACE Data

104 The first image we are processing has been used as a standard in a number of previous publications
 105 [3,4,18,19], which shows coronal loops in a dipolar active region that was recorded by the *TRACE*
 106 spacecraft on 1998 May 5, 22:21 UT, in the 171 Å wavelength (Fig. 1, center). The original image
 107 has a size of 1024×1024 pixels with a pixelsize of $0.5'' (\approx 360 \text{ km on the solar surface})$. The EUV
 108 brightness or intensity in every pixel is quantified by a data number (DN), which has a minimum of 56
 109 DN and a maximum of 2606 DN in this image. We show the bandpass-filtered image (with a lowpass
 110 boxcar of $n_{sm1} = 5$ pixels and a highpass boxcar of $n_{sm2} = 7$ pixels) in Fig. 2. The image shows at
 111 least four different textures (Fig. 1, side panels): coronal loops (L: curvi-linear features), so-called moss
 112 regions (M: high-contrast reticulated or spongy features in the center of the image, which represent
 113 the footpoints of hot coronal loops), transition region emission (T: low-contrast irregular features in the
 114 background), and faint emission areas. The faint image areas show in addition a ripple with diagonal

Figure 1. A solar EUV image of an active region, recorded with the TRACE spacecraft on 1998 May 15, is shown with a colorscale that has the highest brightness in the white regions (center). In addition we show (100×100 pixel) enlargements of four subregions with different textures, which contain coronal loops (top left panel), electronic ripple (bottom left panel), chromospheric and transition region emission (top right panel), and moss regions with footpoints of hot coronal loops (bottom right panel).



115 stripes at a pedestal level of $\approx 57 \pm 1$ DN (Fig. 2 bottom left panel R) that results from some interference
 116 in the electronic readout, which can produce unwanted non-solar structures in the automated detection
 117 of curvi-linear features.

118 The automated detection of curvi-linear features with the OCCULT-2 code yields a total of 437
 119 loop structures with lengths of $L \geq 30$ pixels (Fig. 2), whereof the longer loops (with lengths of
 120 $L \gtrsim 50$) coincide well with the 210 visually/manually traced loops (see Fig.7 in [4]). The good
 121 agreement between the automated and visually detected loops can also be seen from the cumulative
 122 size distributions of loop lengths obtained with both methods (Fig. 1, bottom right panel). The two
 123 methods detect $N = 154$ and $N = 134$ loops with a length of $L \geq 70$ pixels, and both distributions have
 124 a powerlaw slope of $\alpha_L \approx 2.9 \pm 0.1$. Challenges of coronal loop detection in this image are confusion
 125 and interference from all three types of non-loop structures (Fig. 1): chains of "dotted moss structures",
 126 filamentary and spicular transition region emission, and the diagonal stripes of electronic ripple in the
 127 background, which become all comparable with the signal of loop structures once the image contrast is
 128 enhanced with a highpass filter.

129 The successful or false detection in an image thus depends most strongly on the chosen low and
 130 highpass filter constant n_{sm2} and the background base level $z_{min} = z_{med} \times q_{med}$, and to a lesser degree
 131 on the other control parameters. A good indicator of the completeness and efficiency of automated

Figure 2. A bandpass-filtered ($n_{sm1} = 5, n_{sm2} = 7$) version of the original image rendered in Fig. 1 is shown (greyscale), with automated loop tracings overlaid (red curves). Cumulative size distributions $N(> L)$ of loop lengths are also shown (bottom right panel), comparing the automated tracing (red distribution) with visually/manually traced loops (black distribution). The maximum lengths L_m (in pixels) are listed for the longest loops detected with each method.

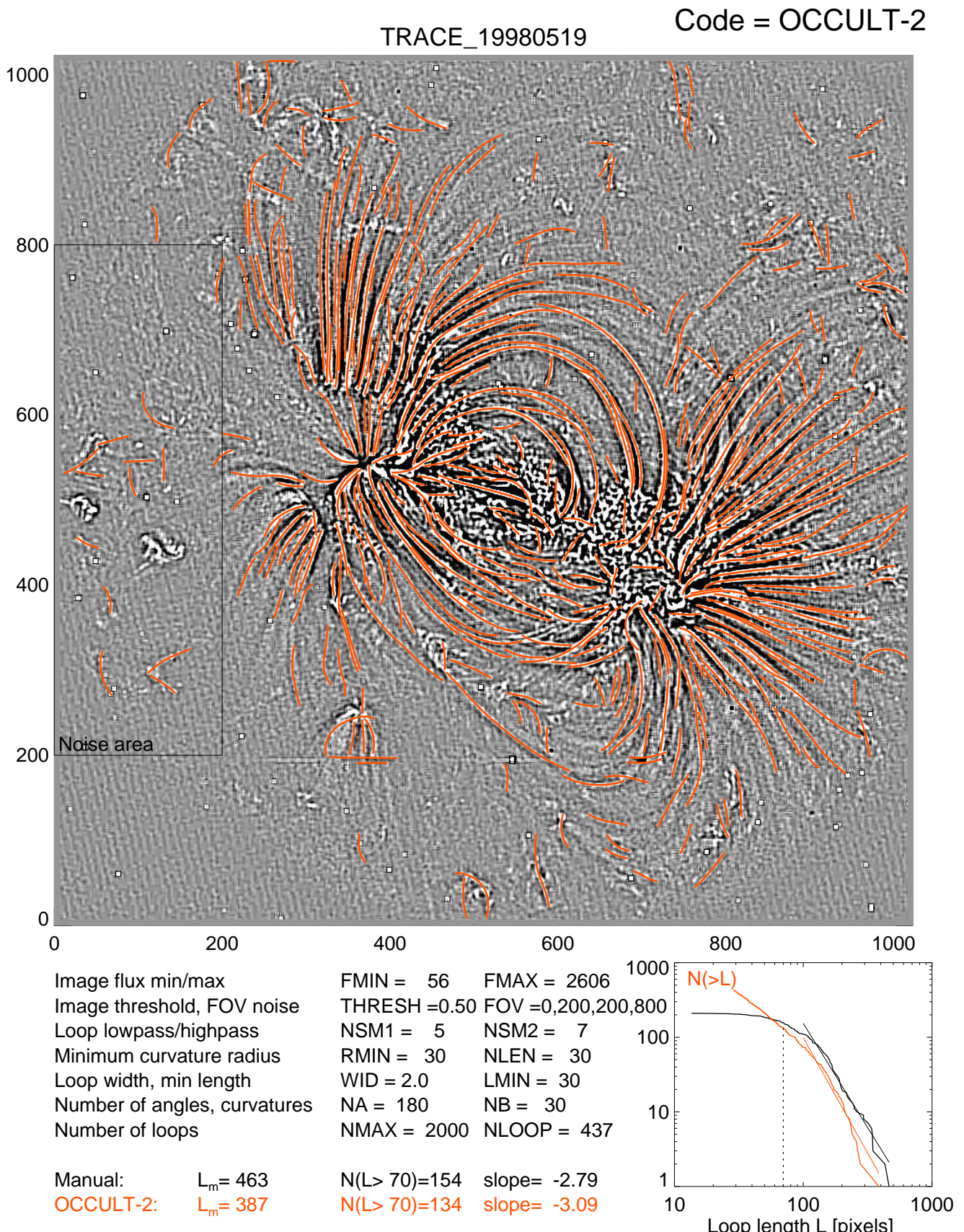
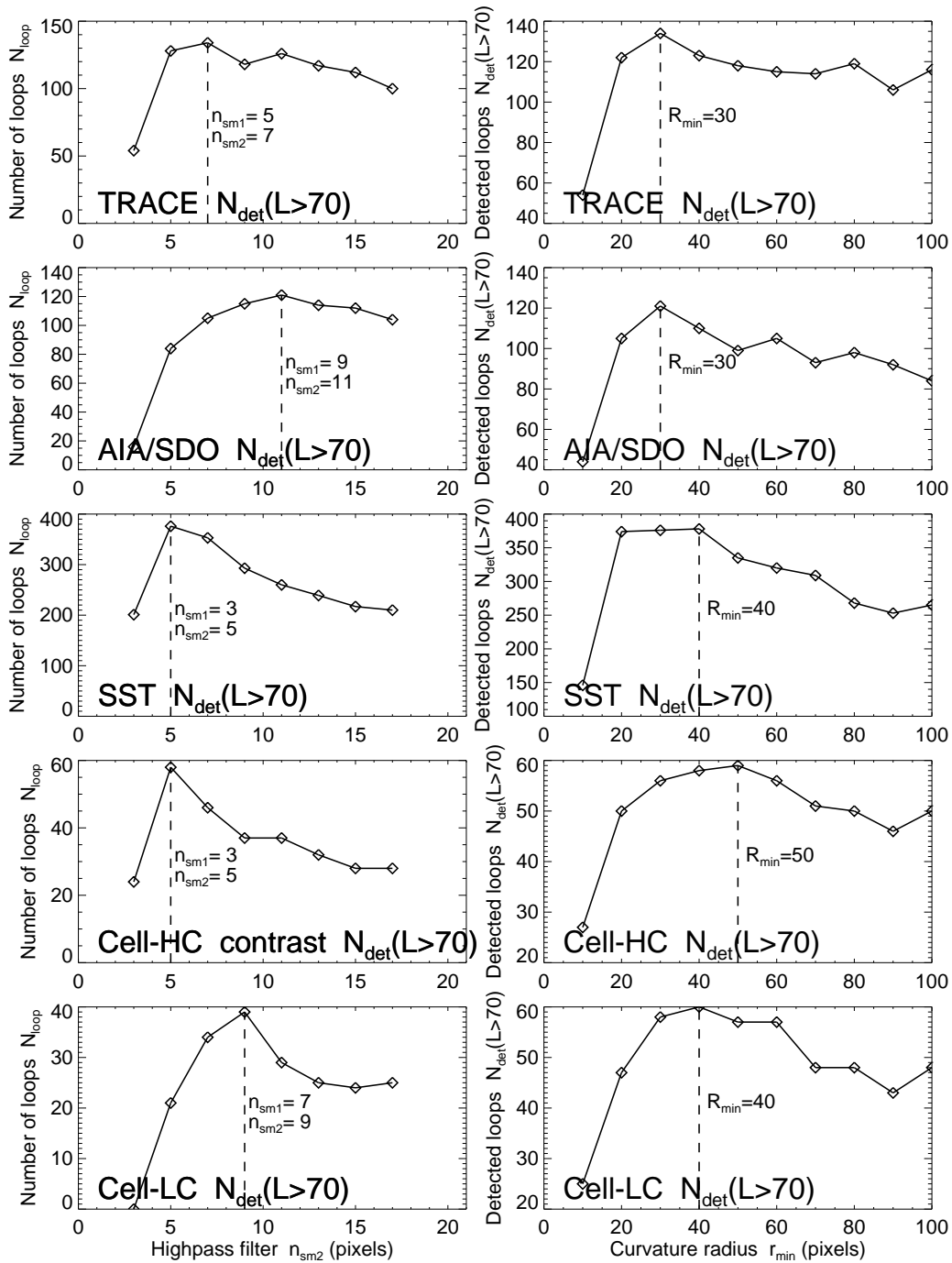


Figure 3. The optimization of the highpass filter constant n_{sm2} (y-axis) is shown for the number of detected loops (with lengths longer than 70 pixels) for all analyzed cases, $N_{det}(L \geq 70)$ (left panels). The optimization of detected loops as a function of the curvature radius r_{min} is also shown (right panels).



132 loop detection is the number of coherently detected long loops, say with a length above 70 pixels here,
 133 $N_{det}(L > 70)$ (which is marked with a dotted line in the size distribution in Fig. 2, bottom right panel). In
 134 Fig. 3 (top left panel) we show how this detection efficiency $N_{det}(n_{sm2})$ varies as a function of the chosen
 135 control parameter n_{sm2} . The detected number has a maximum of $N_{det} = 134$ at $n_{sm1} = 5$ and $n_{sm2} = 7$,
 136 which corresponds to a bandpass filter in the range of 5-7 pixels ($2.5'' - 3.5''$ or 1800-2500 km on the solar
 137 surface). It appears that this is the most typical cross-section width (FWHM) of coronal loops. Other
 138 statistical studies of coronal loops observed with TRACE yield similar values (e.g., FWHM= 1420 ± 340
 139 km; [2]). Thus, if an image contains structures with a preferential cross-section width, the relevant
 140 cross-section range can be bracketed with a bandpass filter (n_{sm1}, n_{sm2}), providing a useful *a priori*
 141 information for automated detection of curvi-linear features. We conducted tests with all possible filter
 142 widths $n_{sm1} = 1, 3, \dots, 21$ and $n_{sm2} > n_{sm1}$ and found that the largest number of detected structures
 143 virtually always occurs at $n_{sm2} = n_{sm1} + 2$, which can be explained also by the theoretical argument that
 144 the best signal-to-noise ratio is obtained for maximum smoothing of the highpass-filtered (unsharp mask)
 145 image. We vary also the minimum curvature radius r_{min} and find a maximum of detected structures at
 146 $r_{min} \approx 30$ pixels (Fig. 3 top right panel).

147 3.2. SDO/AIA Data

148 The next image to which we apply our automated loop tracing code is from the *Atmospheric Imager*
 149 *Assembly (AIA)* onboard the *Solar Dynamics Observatory (SDO)*, which replaced the TRACE mission
 150 and is operating since 2010 [20]. AIA has a similar spatial resolution (pixel size $0.6''$) as TRACE (pixel
 151 size $0.5''$), but covers the full Sun disk, with an image size of 4096×4096 pixels. Fig. 4 shows a subimage
 152 with a size of 1450×650 pixels, which contains a complex of two magnetically coupled active regions,
 153 observed on 2011 Aug 03, 01 UT, in the 171 \AA wavelength. This image is currently subject of nonlinear
 154 force-free magnetic modeling (Mark DeRosa, private communication 2012), and thus requires automated
 155 loop tracing to constrain the coronal part of the magnetic field configuration [5]. Differences to the
 156 TRACE image are the higher sensitivity of the AIA telescopes, different exposure times, the availability
 157 of simultaneous images in 8 other wavelengths, different image compression, and no apparent electronic
 158 ripple in the CCD readout, which all affect the automated detection of faint structures. Synthesized loop
 159 tracings from multiple wavelength filters has been proven to provide a more robust and representative
 160 subset of loop structures for magnetic modeling than loop tracings from a single filter image ([6]).

161 We vary the lowpass filter constant in the range of $n_{sm1} = 1, \dots, 21$, set the highpass filter constant
 162 to $n_{sm2} = n_{sm1} + 2$, and find a maximum detection rate of $N_{det}(L > 70) = 121$ loop structures for
 163 $n_{sm1} = 9$ and $n_{sm2} = 11$ (Fig. 3, second row left panel). We vary also the minimum curvature radius
 164 in the range of $r_{min} = 10, \dots, 100$ pixels and find a maximum detection rate of $N_{det}(L > 70) = 121$ at
 165 $r_{min} = 30$ pixels (Fig. 3, second row right panel).

166 3.3. SST Data

167 Now we apply automated loop tracing to a solar image in a completely different wavelength, namely
 168 in the $H\alpha$ 6563 \AA line, the first line of the Balmer series of hydrogen. Fig. 5 shows such an image of
 169 the solar upper chromosphere, which displays chromospheric spicules in the right side of the picture and

Figure 4. Bandpass-filtered image of an active region complex observed with AIA/SDO on 2011 Aug 3, 01 UT, 171 Å, shown as intensity image (top panel), as bandpass-filtered version with $n_{sm1} = 9$ and $n_{sm2} = 11$ (middle panel), and overlaid with automatically traced loop structures (bottom panel), where the low-intensity values below the median of $f = 75$ DN are blocked out (grey areas).

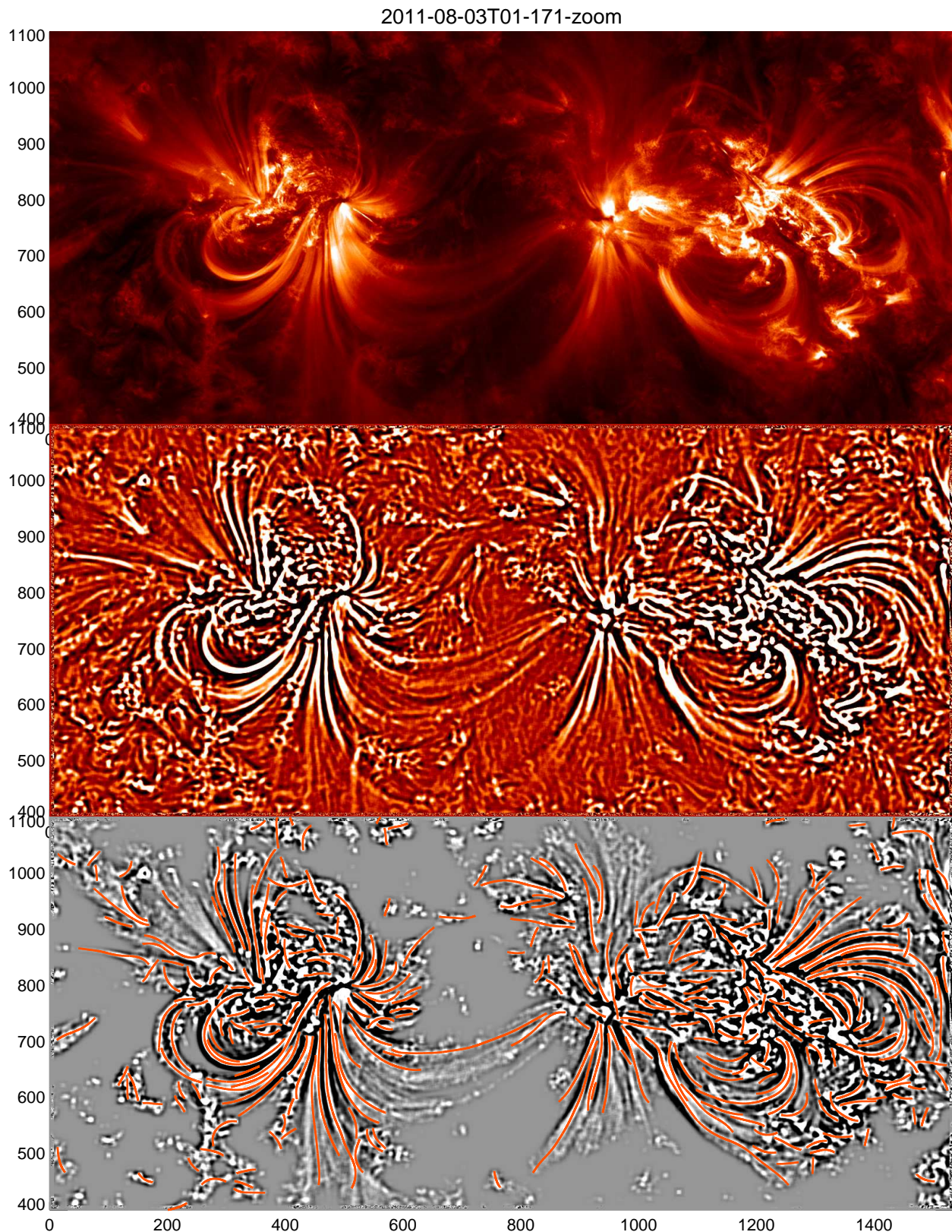
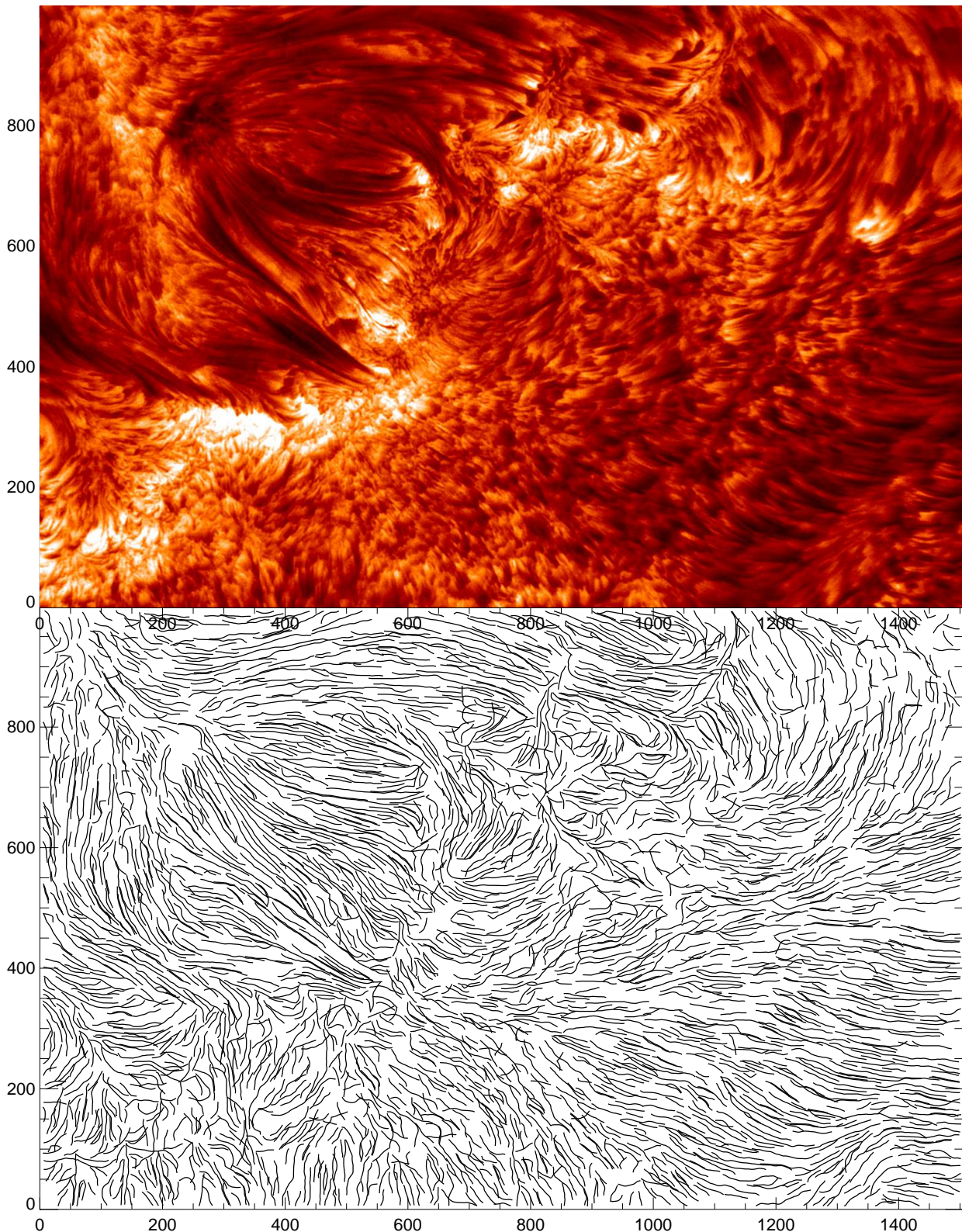


Figure 5. High-resolution image of the solar Active Region 10380, recorded on 2003 June 16 with the Swedish 1-m Solar Telescope (SST) on La Palma Spain (top panel) and automated tracing of curvi-linear structures with a lowpass filter of $n_{sm1} = 3$ pixels, a highpass filter of $n_{sm2} = 5$ pixels, and a minimum curvature radius of $r_{min} = 30$ pixels, tracing out 1757 curvi-linear segments (bottom panel).



170 filamentary structures in the upper chromosphere and transition region (in altitudes $\approx 2000 - 5000$ km
171 above the solar surface) [10,11]. The image was taken with the *Swedish 1-m Solar Telescope (SST)*
172 on La Palma, Spain, using a tunable filter, tuned to the blue-shifted line wing of the $H\alpha$ 6563 Å line.
173 The spicules are jets of moving gas at a lower temperature than the million degree hot corona and flow
174 upward from the chromosphere to the transition region with a speed of ≈ 15 km s⁻¹ [10]. The image has
175 a size of 1507×999 pixels (62×41 Mm on the solar surface), with a pixel size of $0.041''$ (or 30 km on
176 the solar surface). This picture is particularly intriguing for automated tracing of curvi-linear structures
177 because of the ubiquity and complexity of fine structure.

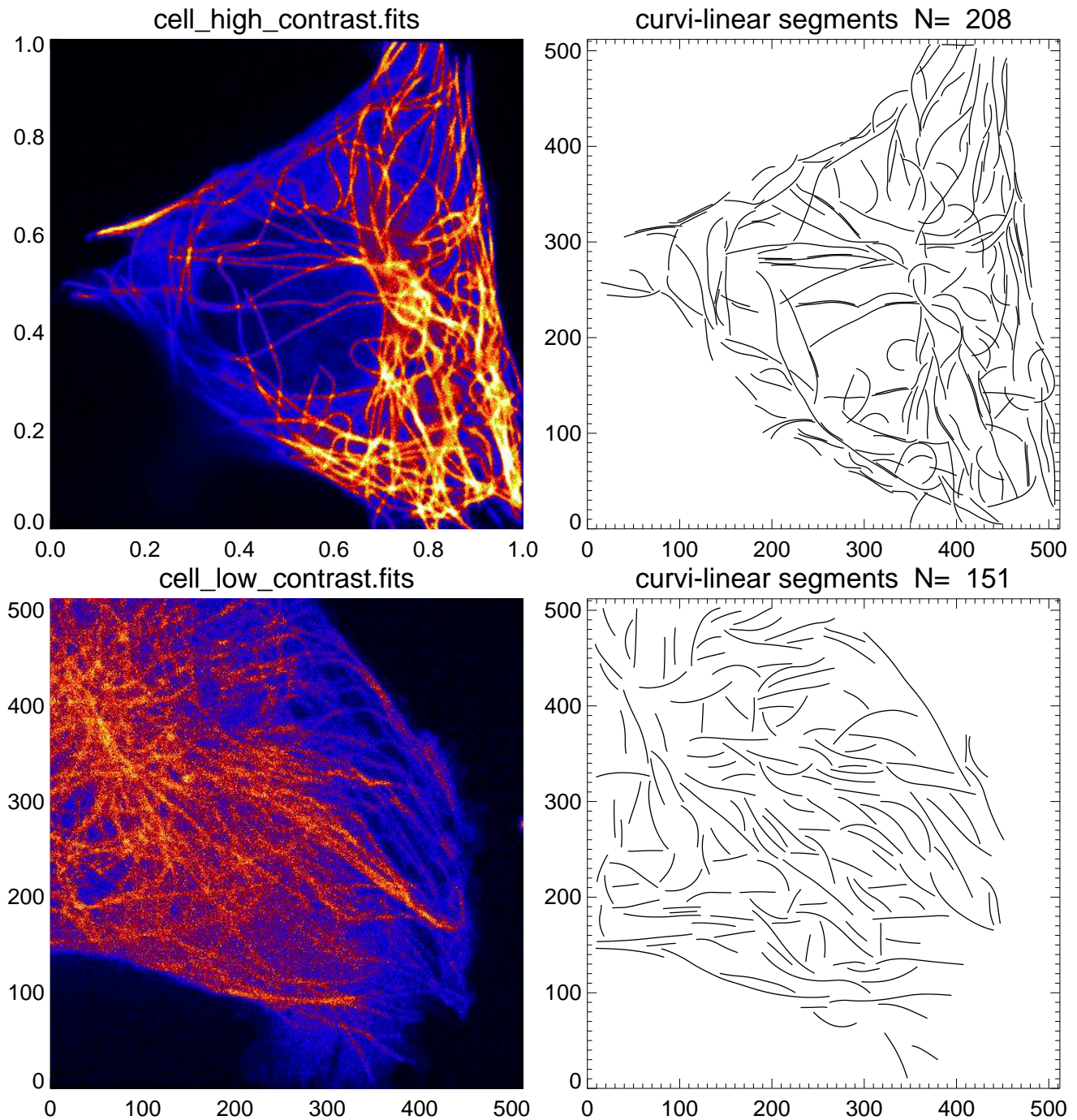
178 This SST image has such a high contrast so that there is no significant noise that affects curvi-linear
179 tracing. Thus, we set the background level to zero ($q_{med} = 0.0$) in the OCCULT-2 code. We vary the
180 lowpass filter constant in the range of $n_{sm1} = 1, \dots, 21$, set the highpass filter constant to $n_{sm2} = n_{sm1} + 2$,
181 and vary the minimum curvature radius in the range of $r_{min} = 10, \dots, 100$ pixels. We find a maximum
182 number of detected structures of $N_{det}(L > 70) = 376$ (with a length above 70 pixels) at $n_{sm1} = 3$
183 and $n_{sm2} = 5$ (Fig. 3, middle row left panel), and $r_{min} = 40$ pixels (Fig. 3, middle row right panel).
184 Extending to shorter segments with lengths of $L > 30$ pixels, the automated tracing code identifies a total
185 of 1757 curvi-linear segments, which outline the patterns of the flow field in the upper chromosphere
186 (Fig. 5, bottom panel).

187 **4. Applications to Biophysics**

188 Finally we apply our automated tracing code to images obtained in cellular biophysics, in order to test
189 the versatility and universality of the OCCULT-2 code. As an example, we chose microscopy images of
190 microtubules, but the same approach could be applied to any other filament-like structures: intermediate
191 or actin filaments, fibrin, etc. Microtubules are long stiff polymers that are part of cytoskeleton (internal
192 cellular scaffolding). They are important for cell division, motility and organization ([16], [9]). The
193 entangled network of microtubules serves as a “railroad” system for delivery of cargos by molecular
194 motors and also as a stiff carcass controlling cellular mechanics ([9], [26]). It is a dynamic network
195 adapting and changing in time in response to external cues. The automated extraction of the microtubules
196 network’s configuration from microscopy images and movies can provide insights on the mechanisms of
197 these changes.

198 Fig. 6 shows two images of cells from two different cell lines with microtubules networks of different
199 density. Cells belonging to CHO cell line (Fig. 6 top, image Cell-HC) are small and have sparse
200 microtubule network. Cells from U2OS line (Fig. 6 bottom, image Cell-LC) are larger and contain
201 more dense radial network. Since microtubules are transparent to the visible light, a fluorescent tag is
202 used to observe them in the living cells. In the analyzed images (Fig. 6) microtubules were labeled
203 with a green fluorescent protein (GFP) ([28]) that adsorbs light at 490 nm and has an emission peak
204 at 510 nm wavelength. The images were acquired with a spinning disk confocal microscope using the
205 corresponding GFP’s emission filter. The magnified image was projected on the 16-bit chip of camera
206 with dimensions of 512×512 pixels resulting in the final image pixel size of 66 nm. The width of
207 microtubules filaments measured in the electron microscopy studies is about 25 nm ([29]). Due to the
208 diffraction limit the effective width of microtubules in the image is much larger and is defined by the

Figure 6. False-coloured images of microtubule filaments in live cells: a high-contrast image of CHO cell (top left panel, Cell-HC), a low-contrast image of U2OS cell (bottom left panel; Cell-LC). The size of the images corresponds to $34 \mu\text{m}$. The automated curvi-linear tracing of both images was carried out with the parameters: $n_{sm1} = 3$, $n_{sm2} = 5$, and $r_{min} = 15$ for Cell-HC, and $n_{sm1} = 7$, $n_{sm2} = 9$, and $r_{min} = 30$ for Cell-LC.



209 microscopy setup and the wavelength used ([1]). In our case it is approximately equal to a half of the
 210 emission wavelength (510 nm) that is close to the measured microtubule width of 4.7 ± 2.0 pixels. The
 211 two pictures shown in Fig. 6 (left) show cases of opposite contrast, one with high contrast (Fig. 6 top,
 212 image Cell-HC), and one with low contrast (Fig. 6 bottom, image Cell-LC). The difference in contrast
 213 is explained by a different amount of GFP fluorescent tag associated with microtubules. The automated
 214 tracing of the cell filaments provides their locations inside cell and curvature radii, from which flexural
 215 rigidity and mechanical stress can be inferred.

216 We optimize the automated filament tracing by varying the bipass filter constants and find a maximum
 217 number of detected filaments (with lengths $L > 70$ pixels) with $n_{sm1} = 3$, $n_{sm2} = 5$, $r_{min} = 50$ for the
 218 high-contrast cell image, and $n_{sm1} = 7$, $n_{sm2} = 9$, $r_{min} = 40$ for the low-contrast cell image (Fig. 3).
 219 The low-contrast image has a higher degree of noise, and thus the filter constants have to be adjusted to
 220 a larger value for the low-contrast cell image ($n_{sm1} = 7$) than for the high-contrast image ($n_{sm1} = 3$).

221 5. Discussion and Conclusions

222 5.1. Optimization of Automated Curvi-Linear Tracing

223 The efficiency and accuracy of automated curvi-linear tracing can be controlled by a number of tuning
 224 or control parameters. For the present OCCULT-2 code we have three independent control parameters
 225 (n_{sm1} , r_{min} , q_{med}). A prerequisite for the application of curvi-linear tracing codes is the assumption that
 226 the structures of interest have a much smaller width w than their length l , so that they can be represented
 227 by a 1D path, which is generally curved, possibly limited by a minimum curvature radius r_{min} . The larger
 228 the minimum curvature radius is, the less ambiguity there is for tracing of crossing 1D structures. In this
 229 study we explored the parameter space of the control parameters n_{sm1} and r_{min} in order to optimize the
 230 performance of the automated tracing code.

231 The lowpass filter (n_{sm1}) and highpass filter (n_{sm2}) represent the brackets or scale range of a bandpass
 232 filter, bracketing the range of cross-sections of detected structures. We expect to find structures with the
 233 smallest width preferentially in images with a high signal-to-noise ratio, while noisy images require
 234 more smoothing to enhance fine structure, and thus tend to have larger widths due to the smearing effect
 235 of the smoothing. We found the narrowest structures indeed in the two images with the highest contrast
 236 (i.e., the SST and Cell-HC image), where highpass filters with boxcars of $n_{sm2} = 5$ pixels were used.
 237 In images with lower contrast, optimum performance occurred for highpass filters of $n_{sm1} = 7, \dots, 11$
 238 pixels. In addition, we found that the smallest bandpass filters produce the sharpest structures and thus
 239 the highest detection rate of structures. Since a symmetric boxcar requires odd numbers $n_{sm} = 1, 3, 5, \dots$,
 240 the smallest difference between a lowpass and a highpass filter is 2, and thus the optimum combination
 241 is expected to be $n_{sm2} = n_{sm1} + 2$, which we indeed confirmed also experimentally.

242 For the minimum curvature radius we found optimum performance for a typical range of $r_{min} \approx$
 243 $30, \dots, 50$ pixels (Fig. 3), which seems not to depend on the contrast of the image.

244 The control parameter $q_{med} = 1$ suppresses faint structures in an image that are below the median
 245 value of the image brightness. A meaningful value for this parameter depends very much what fraction
 246 of the image contains bright structures of interest, which has to be decided depending on the area ratio

247 of structures of interest to non-relevant background area. If the background has comparable brightness
248 to the structures of interest, a thresholded separation may be impossible, but may still succeed if the
249 background has a different texture than the curvi-linear features (see examples in Fig. 1, where moss and
250 transition region emission have a different texture than coronal loops, while background ripples have
251 the same texture as straight loops and can only be separated by a threshold control parameter). Future
252 efforts aim to synthesize the loop tracings from multi-wavelength image sets, which are more robust and
253 representative for magnetic modeling than single-wavelength images ([6]).

254 In conclusion, we recommend the following procedure to achieve optimum performance of the curvi-
255 linear tracing code (OCCULT-2): (1) Start with the following recommended control settings: $n_{sm1} = 1$,
256 $n_{sm2} = 3$, $r_{min} = 30$, and $q_{med} = 1.0$; (2) Vary the filter combination in the range of $n_{sm1} = 1, 3, \dots, 15$,
257 while setting $n_{sm2} = n_{sm1} + 2$, to find the maximum detection rate for a given loop length (e.g., here
258 we used $L > 70$ pixels); (3) Low-contrast images are likely to require higher highpass filter values
259 n_{sm2} than high-contrast images. (4) Vary the minimum curvature radius r_{min} within some range to find
260 the maximum detection rate of structures; (5) If the code yields a lot of random structures in obvious
261 background areas, increase the base level factor $q_{med} > 1$.

262 The software of the numerical code OCCULT-2 is publicly accessible in the *Interactive Data Language*
263 (*IDL*) in the *Solar Software (SSW)* package. A tutorial and example is accessible at the authors
264 homepage <http://lmsal.com/~aschwand/software/>.

265 5.2. Solar Applications

266 The automated tracing of curvi-linear structures in solar physics has mostly been applied to
267 extreme-ultraviolet or soft X-ray images, which show magnetized coronal loops that outline the coronal
268 magnetic field, due to the low plasma- β parameter in the solar corona (which is defined as the ratio of
269 the thermal to the magnetic pressure). Thus, coronal loops represent the perfect tracers of the otherwise
270 invisible coronal magnetic field. Standard magnetic field models of the solar corona or parts of it, such
271 as sunspot regions and active regions, have been modeled by extrapolating a photospheric magnetogram,
272 either with a potential field solution or a force-free solution of Maxwell's equations. However, since
273 the chromosphere was found not to satisfy the force-free condition [23], extrapolations of photospheric
274 magnetograms do not exactly render the coronal magnetic field, while coronal loops outline the true
275 coronal magnetic field. It is therefore desirable to trace such coronal loops in EUV and soft X-ray images
276 and to use them to constrain a magnetic field solution. Such attempts have been performed with single
277 EUV images as well as with stereoscopic EUV image pairs [5]. Forward-fitting of theoretical magnetic
278 field models to traced coronal loops is able to discriminate between potential field and force-free field
279 models, as well as to quantify the free magnetic energy (that is released in solar flares) and Lorentz
280 forces, e.g., [13]. Curvi-linear tracing of filamentary structures in the chromosphere and transition region
281 (Fig. 5) may also help to constrain the horizontal magnetic field components in the non-forcefree regions,
282 which has been used in pre-processing of solar force-free magnetic field extrapolations [12].

283 One fundamental limitation of automated coronal loop tracing is the confusion by background
284 structures resulting from EUV emission from the transition region, which has generally a cooler
285 temperature than the coronal loops. Future efforts may use multi-wavelength image data sets to

discriminate EUV emission from the chromosphere, transition region, and the corona by its temperature, using a deconvolution of the multi-wavelength temperature filter response functions in terms of a differential emission measure (DEM) method.

5.3. Biological Applications

The method of curvi-linear tracing is increasingly used in the analysis of biological and medical images, such as to characterize blood vessel tracking in retinal images [15,21,27], neurons [30], dendritic spines [31], or microtubule tracing in fluorescent and phase-contrast microscopy [8,17,25], as shown in Fig. 6. In our experiment with a high-contrast (Fig. 6, top panel) and low-contrast image (Fig. 6, bottom panel), we demonstrated that a bypass or bandpass filter with a bandpass factor of $n_{sm2} = n_{sm1} + 2$ enhances the structures to an optimum contrast for automated tracing. Moreover we found that the bandpass filter of low-contrast images requires a larger width ($n_{sm2} = 9$ pixels in Fig. 6, bottom panel) than in a high-contrast image ($n_{sm2} = 5$ pixels in Fig. 6, top panel).

In our optimization exercise we concentrated mostly on the completeness of detected long curvi-linear segments, but future efforts may also consider the optimization of linking multiple segments that are interrupted with gaps or subject to crossings. The efficiency and reliability of automated curvi-linear algorithms became more important with the massive increase of imaging data over the last decade, which exceeds our limited capabilities of visual inspection. Note that the algorithm used here tracks curvi-linear structures that differ by 16 orders of magnitude in size, from 66 nm to 360 km (pixel size in images).

6. Appendix A: Analytical Description of the OCCULT-2 Code

The *Oriented Coronal CURved Loop Tracing (OCCULT-2)* code version 2 is an improved version of the original OCCULT code described in Aschwanden (2010). The improvements include: (1) a “curved” guiding segment that is adjusted to the local curvature radius of a traced loop (representing the second-order term of a polynomial), rather than the linear (first-order polynomial) guiding segment used in the original version, (2) suppression of faint structures, (3) bypass filtering instead of highpass filtering, and (4) simplification of selectable free parameters.

The input is a simple 2-dimensional (2D) image z_{ij} , with pixel numbers $i = 0, \dots, n_x - 1$ on the x-axis, and $j = 0, \dots, n_y - 1$ on the y-axis, respectively. The output is a number of curvi-linear structures (also called “loops” for short), which are parameterized in terms of x and y-coordinates, $[x(s_k), y(s_k)]$, where the loop length coordinate $s_k = 0, \dots, n_s$ is given in steps of $\Delta s = 1$ pixel, so that for all $k = 0, \dots, n_s - 1$,

$$\Delta s_k = \sqrt{([x(s_k) - x(s_{k-1})])^2 + [y(s_k) - y(s_{k-1})]^2)} = 1, \quad k = 0, \dots, n_s - 1, \quad (2)$$

with n_s the number of loop points for each loop.

The goal of the algorithm OCCULT-2 is to retrieve as many curvi-linear structures as possible, without picking up false signals of non-existing structures in the noise of the image, which has some probability to form chains of random points in a curved array configuration. The challenges are therefore to evaluate an optimum threshold level that separates existing loops from noise structures, and to retrieve the real curvi-linear structures as completely as possible, without subdividing them into partial loop segments.

Our strategy to obtain a fast numeric code is to retrieve the loops in a one-dimensional search algorithm, because any two-dimensional concept has a computation time that grows with the square of the image size. The one-dimensional parameter space is essentially the loop length coordinate s_k , $k = 0, \dots, n_s - 1$. In addition we define two other independent parameters in each loop point, which can be considered as the first-order and second-order term of a polynomial, namely the local direction angle α_l , $l = 0, \dots, n_\alpha$, and the curvature radius r_m , $m = 0, \dots, n_r$. The algorithm selects iteratively the brightest position (x_i, y_j) in the image and starts a bi-directional loop tracing, determining first the local direction $\alpha_l(x_i, y_j)$ and curvature radius $r_m(x_i, y_j)$ at the starting point, and continues tracing the loop within a small (guided) range of the local curvature radius, which is the principle of “orientation-guided tracing”. So we are dealing essentially with 1D-tracing in a 5D-parameter space $(x_i, y_j, s_k, \alpha_l, r_m)$, which we parameterize with the 5 indices (i, j, k, l, m) that have the index ranges $i = 0, \dots, n_x - 1$, $j = 0, \dots, n_y - 1$, $k = 0, \dots, n_s$, $l = 0, \dots, n_\alpha$, $m = 0, \dots, n_r$. Specifically, we define the arrays,

$$s_k^{bi} = \Delta s \left(k - \frac{n_s}{2} \right), \quad k = 0, \dots, n_s - 1, \quad (3)$$

for a symmetric bi-directional array, used in the search of the local direction α_l , and

$$s_k^{uni} = \Delta s k, \quad k = 0, \dots, n_s - 1, \quad (4)$$

for a uni-directional array, used in the search for the curvature radius in the forward-direction of a traced structure. For the directional angle α_l , which is only determined at the starting point of the loop, we use a fixed array with a resolution of one degree (or $\pi/180$ radian),

$$\alpha_l = \pi \left(\frac{l}{n_\alpha} \right), \quad l = 0, \dots, n_\alpha, \quad n_\alpha = 180. \quad (5)$$

For the curvature radii r_m we use a reciprocal scaling in order to obtain a uniform distribution of directional angles at the end of a curvature segment,

$$r_m = \frac{r_{min}}{[-1 + 2m/(n_r - 1)]}, \quad n_r = 30. \quad (6)$$

313 This parameterization covers positive and negative curvature radii in the ranges of $[-\infty, -r_{min}]$ and
314 $[r_{min}, +\infty]$. The choice of an even number n_r prevents the singularity $r_m = \pm\infty$.

315 Now we describe the consecutive steps of the algorithm one by one, which follow more or less the
316 same flow chart as depicted in Figure 1 of Aschwanden (2010).

(1) Image base level (q_{base}): If the image consists of high-contrast structures without unwanted secondary structures in the background, we do not have to worry about the image base level and can set it to the lowest value (which should be zero or positive in astrophysical images that record an intensity or brightness). However, if there are unwanted structures at a faint brightness level, we can just set the image base level z_{base} above the brightness level of unwanted structures, which we parameterize with the factor q_{med} in units of the median brightness level $z_{med} = median[z_{i,j}]$,

$$z_{base} = z_{med} \times q_{base}, \quad (7)$$

so that the corrected brightness $z'_{i,j}$ in each pixel fulfills the condition

$$z'_{i,j} \geq z_{base}. \quad (8)$$

317 For $q_{med} = 0$ the image is unchanged, while the image $z'_{i,j}$ appears to be flat in the fainter half area of the
 318 image, if set $q_{med} = 1.0$. So, the value q_{med} can be adjusted depending on the estimated fraction of the
 319 image that is covered with structures of interest. For solar images, this feature offers a convenient way
 320 to filter out coronal loops in active regions (which are bright) from unwanted structures in the Quiet Sun
 321 (which are faint).

(2) Bandpass Filtering (n_{sm1}, n_{sm2}): The tracing of curvi-linear structures is considerably eased by enhancing of fine structures within a chosen bandpass that corresponds to the typical width n_w of structures of interest, which is typically a few pixels, and assuming that the curvi-linear structures has a much longer length n_s than width, i.e., $n_s \gg n_w$. We accomplish the enhancement with a bandpass filter, which consists of a lowpass filter with a boxcar n_{sm1} and a highpass filter with a boxcar n_{sm2} ,

$$z_{i,j}^{filter} = smooth[z'_{i,j}, n_{sm1}] - smooth[z'_{i,j}, n_{sm2}], \quad (9)$$

which filters out broad structures with widths $n_w \gtrsim n_{sm2}$ (highpass filter), but smoothes out fine structure with a boxcar of $n_{sm1} < n_{sm2}$. We experimented with a large number of combinations (n_{sm1}, n_{sm2}) and found that the optimum choice is,

$$n_{sm2} = n_{sm1} + 2, \quad (10)$$

322 which follows the principle of maximum possible smoothing of fine structures with a given width n_{sm2} .
 323 The values for the smoothing with a symmetric boxcar has to be an odd integer, i.e., $n_{sm1} = 1, 3, 5, \dots$,
 324 which implies $n_{sm2} = 3, 5, 7, \dots$, where the lowest value $n_{sm1} = 1$ corresponds to the original image
 325 without any smoothing. This experimentally tested relationship for the optimum choice of bandpass
 326 filters (n_{sm1}, n_{sm2}) reduces also the possible parameter space by one dimension, and thus we have search
 327 only for $n_{sm1} = 1, 3, 5, \dots$, while using $n_{sm2} = n_{sm1} + 2$.

(3) Noise Threshold: Our algorithm starts with the brightest curvi-linear structure and proceeds to fainter structures, and thus we have to find a stop criterion that halts the procedure when it reaches the level of data noise. Such a noise threshold has to be determined empirically for every image, since there are many sources of possible data noise. Testing many images with completely different data types, we found that a most reasonable threshold level can be determined by an interactive choice of a noise area in the image that contains typical data noise but little structures of interest. Such an image area can be characterized by the pixel ranges ($i_{n1} : i_{n2}, j_{n1} : j_{n2}$). In this noise area we determine the median brightness z_{med}^{noise} and define a noise threshold at the doubled value,

$$z_{thresh} = 2 \times (z_{med}^{noise} > 0), \quad (11)$$

328 using only the pixels with positive values in the noise area (in order to prevent a too low value of $z_{thresh} =$
 329 0 in the case when more than 50% of the noisy pixels are below the previously chosen base value z_{base}).
 330 The rationale for the factor 2 in the threshold level comes from the fact that the median separates out
 331 only half of the noisy pixels, while the double value would separate out all noisy pixels if the distribution
 332 of noisy pixel values follows a linear relationship.

(4) Start of Curvi-Linear Structures: We are ready now to trace the first curvi-linear structure. We determine the location (i_0, j_0) of the absolute brightness maximum z_0 in the bandpass-filtered image $z_{i,j}^{filter}$,

$$z_0 = z(x_0, y_0) = max[z_{i,j}^{filter}(x_i, y_j)]. \quad (12)$$

333 The rationale for the choice of this starting point is the expectation to trace first the most significant
 334 structure in the bandpass-filtered image, which can then be continued by going to the next-significant
 335 structure, once the tracing of the first structure has been successfully completed and the corresponding
 336 loop area is eliminated in a residual image. Consequently, the maximum of the brightness in the residual
 337 image marks the second-brightest structure and we can repeat the same procedure by tracing the next
 338 loop.

(5) Loop Direction at Starting Point: The next element of the structure to be traced is the first-order term of a polynomial, the direction angle α_l , which is also the direction of a possible ridge that outlines the local segment of the structure. We determine this directional angle simply by measuring the flux averaged over a straight loop segment symmetrically placed over the starting point (i_0, j_0) and rotated over a full range of possible angles α_l from 0° to 180° degrees. The x,y-coordinates of this linear segment are, with the array s_k^{bi} defined by Eq. (5),

$$x_{k,l} = i_0 + s_k^{bi} \cos \alpha_l, \quad (13)$$

$$y_{k,l} = j_0 + s_k^{bi} \sin \alpha_l, \quad (14)$$

where the index k runs along the length s_k of the segment, and the index l denotes a particular angle α_l . Among the set of angular values α_l we determine the maximum of the summed flux in each rotated segment,

$$z_{max}(\alpha_l) = \max_l \left[\frac{1}{n_s} \sum_{k=0}^{n_s-1} z^{filter}(x_{k,l}, y_{k,l}) \right], \quad (15)$$

339 which yields the local direction $\alpha_{max} = \alpha_l(l = l_{max})$. In the ideal case of a straight ridge with a constant
 340 value z_0 along the ridge segment with length n_s pixels and zero-values outside, a value of $z_{||} = z_0$ is
 341 found, while the value for a segment in perpendicular direction to the ridge is much smaller, namely
 342 $z_{\perp} = 1/n_s$. This ridge criterion works even for a close succession of parallel ridges, in which case it is
 343 still a factor of 2 smaller than in parallel direction, i.e., $z_{\perp} = 1/2$.

(6) Local curvature radius: Next we determine the second-order term of a polynomial that follows the loop to be traced. We define a directional angle β_0 that is in perpendicular direction to the loop and defines the direction where all centers of possible curvature radii are located (that intersect the structure at location (x_0, y_0)), see geometric definition of the angles α and β in Fig. 7,

$$\beta_0 = \alpha_0 + \frac{\pi}{2}. \quad (16)$$

The location (x_c, y_c) of the curvature center with a minimum curvature radius r_{min} is then found at,

$$x_c = x_0 + r_{min} \cos \beta_0, \quad (17)$$

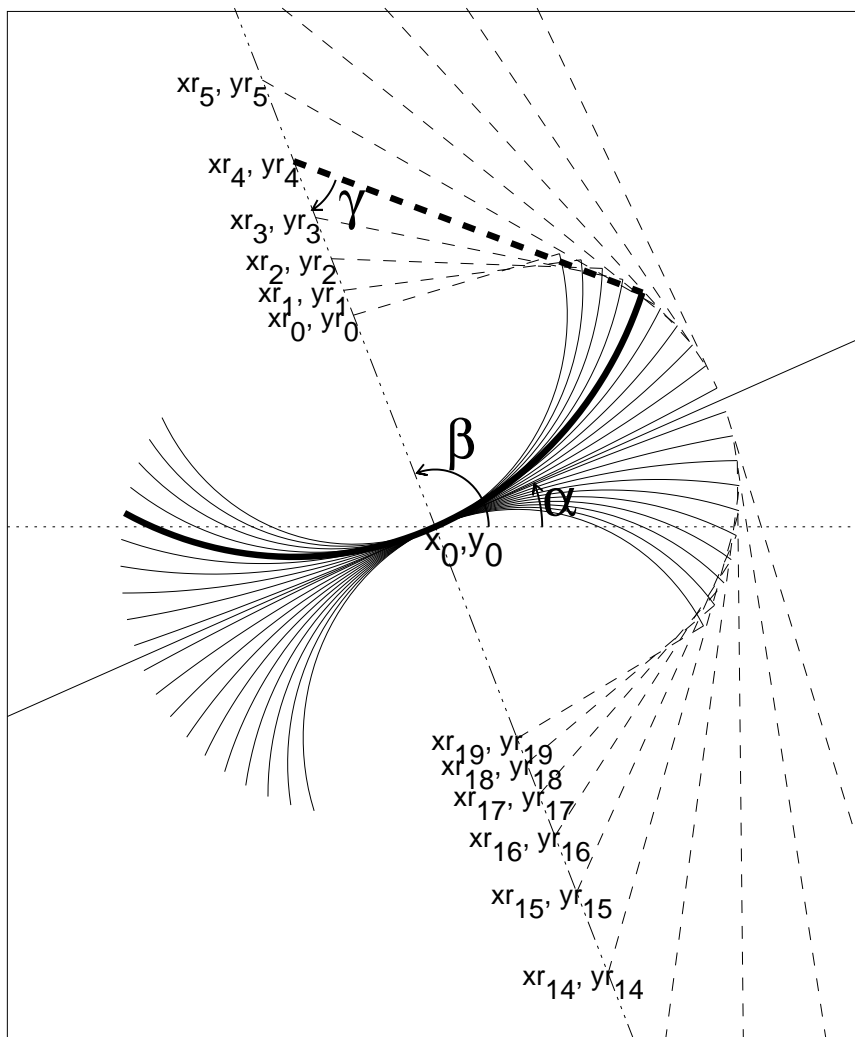
$$y_c = y_0 + r_{min} \sin \beta_0. \quad (18)$$

The loci of all curvature centers (x_m, y_m) of a set of curvature radii $r_m = r_{min}/[-1 + 2m/(n_r - 1)]$ (Eq. 6) is then found at,

$$x_m = x_0 + (x_c - x_0) \frac{r_m}{r_{min}}, \quad (19)$$

$$y_m = y_0 + (y_c - y_0) \frac{r_m}{r_{min}}. \quad (20)$$

Figure 7. Geometry of curvature radii centers (xr_m, yr_m) located on a line at angle β (dash-dotted line), perpendicular to the tangent at angle α (solid line) that intersects a curvi-linear feature (thick solid curve) at position (x_0, y_0) . The angle γ indicates the half angular range of the curved guiding segment (thick solid line).



Since we want to follow a loop along a curved segment for every possible curvature radius r_m , we determine the coordinates for each segment point s_k . It is useful to define the angle β_m of the line that connects a curvature center (x_m, y_m) with a curved segment point s_k ,

$$\beta_m = \beta_0 + \sigma_{dir} \left(\frac{s_k}{r_m} \right), \quad (21)$$

where $\sigma_{dir} = \pm 1$ has two opposite signs, depending on the forward or backward tracing of a loop. The x,y-coordinates (x_{km}, y_{km}) of the loop segment s_k is then,

$$x_{km} = x_m - r_m \cos(\beta_m), \quad (22)$$

$$y_{km} = y_m - r_m \sin(\beta_m). \quad (23)$$

In order to determine the curvature radius r_m that fits the local loop segment best, we search for the segment with the maximum flux along the curve with radius r_m ,

$$z_{max} = \max_m \left[\frac{1}{n_r} \sum_{k=0}^{n_s-1} z'_{i,j}(x_{km}, y_{km}) \right]. \quad (24)$$

Since we know now the optimum curvature radius r_m , we can trace the loop incrementally by a step Δs and extrapolate the position (x_{k+1}, y_{k+1}) and angle α_{k+1} by

$$\alpha_{k+1} = \alpha_k + \sigma_{dir} \frac{\Delta s}{r_m}, \quad (25)$$

$$\alpha_{mid} = \frac{(\alpha_k + \alpha_{k+1})}{2}, \quad (26)$$

$$x_{k+1} = x_k + \Delta s \cos[\alpha_{mid} + (\pi/2)(1 + \sigma_{dir})], \quad (27)$$

$$y_{k+1} = y_k + \Delta s \sin[\alpha_{mid} + (\pi/2)(1 + \sigma_{dir})]. \quad (28)$$

344 **(7) Bidirectional tracing:** The step (6) describes the extrapolation or tracing of the loop segment from
 345 position $s_k = (x_k, y_k)$ to $s_{k+1}(x_{k+1}, y_{k+1})$ by an incremental length step Δs . This step is repeated,
 346 starting from some arbitrary starting point s_0 inside the segment until the first endpoint $s_{n_{s1}}$, where the
 347 traced curvi-linear structure seems to end. The first endpoint generally is demarcated at a location where
 348 the bandpass-filtered image has zero or negative values, so one could just detect the first image pixel
 349 along the guiding segment s_k that is non-positive. However, in order to allow for some minor gaps in
 350 noisy structures, it turned out to be more reliable to define a stop criterion when a least a few pixels
 351 have a nonpositive value, say $n_{gap} = 3$ pixels. An example of a traced loop is shown in Fig. 8, which
 352 illustrates that a loop can reliably be traced even in the presence of secondary loops that intersect at small
 353 angles.

354 After completing the first half segment ($\sigma_{dir} = +1$), we repeat the same procedure from the midpoint
 355 (x_0, y_0) in opposite direction ($\sigma_{dir} = -1$), until we stop at the second endpoint at $s_{n_{s2}}$. We combine than
 356 the two segments $[s_0, s_{n1}]$ and $[s_0, s_{n2}]$ by reversing one segment in order to maintain the same direction,
 357 and concatenating the two equal-directed segments into a single loop structure with indices $[s_0, \dots, s_{n_s}]$,
 358 where the length is $s_n = (s_{n1} + s_{n2})$.

Figure 8. Example of loop tracing in the pixel area [525:680, 453:607] of the image shown in Fig. 2. Loop #19 is traced (blue crosses) over a length of 115 pixels (orange numbers), crossing another structure at a small angle. The curves at position 115 indicate the three curved segments that have been used in the tracing of the last loop point. The black contours indicate the bandpass-filtered difference image, and the red contours indicate the previously traced and erased structures in the residual difference image.

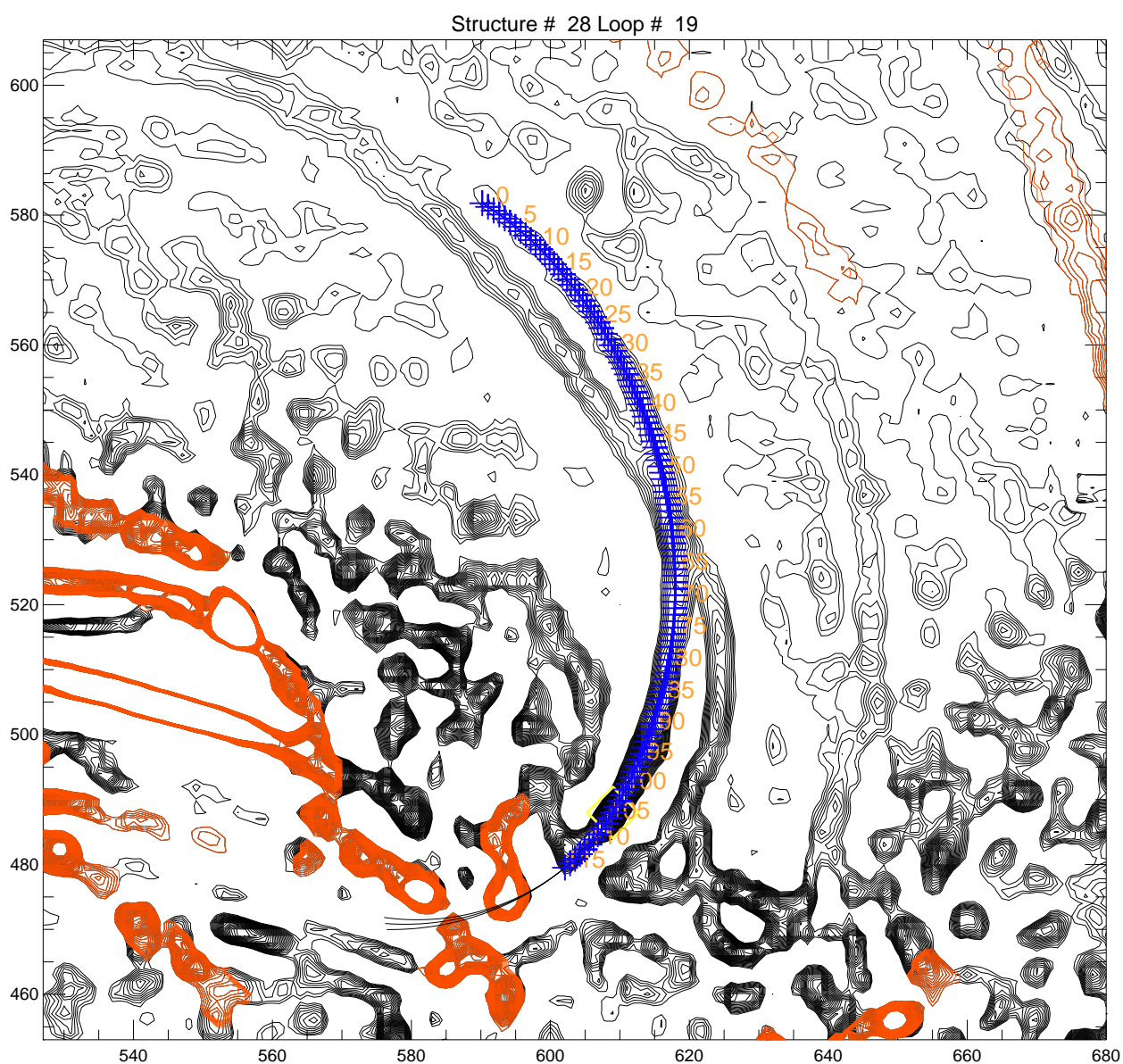
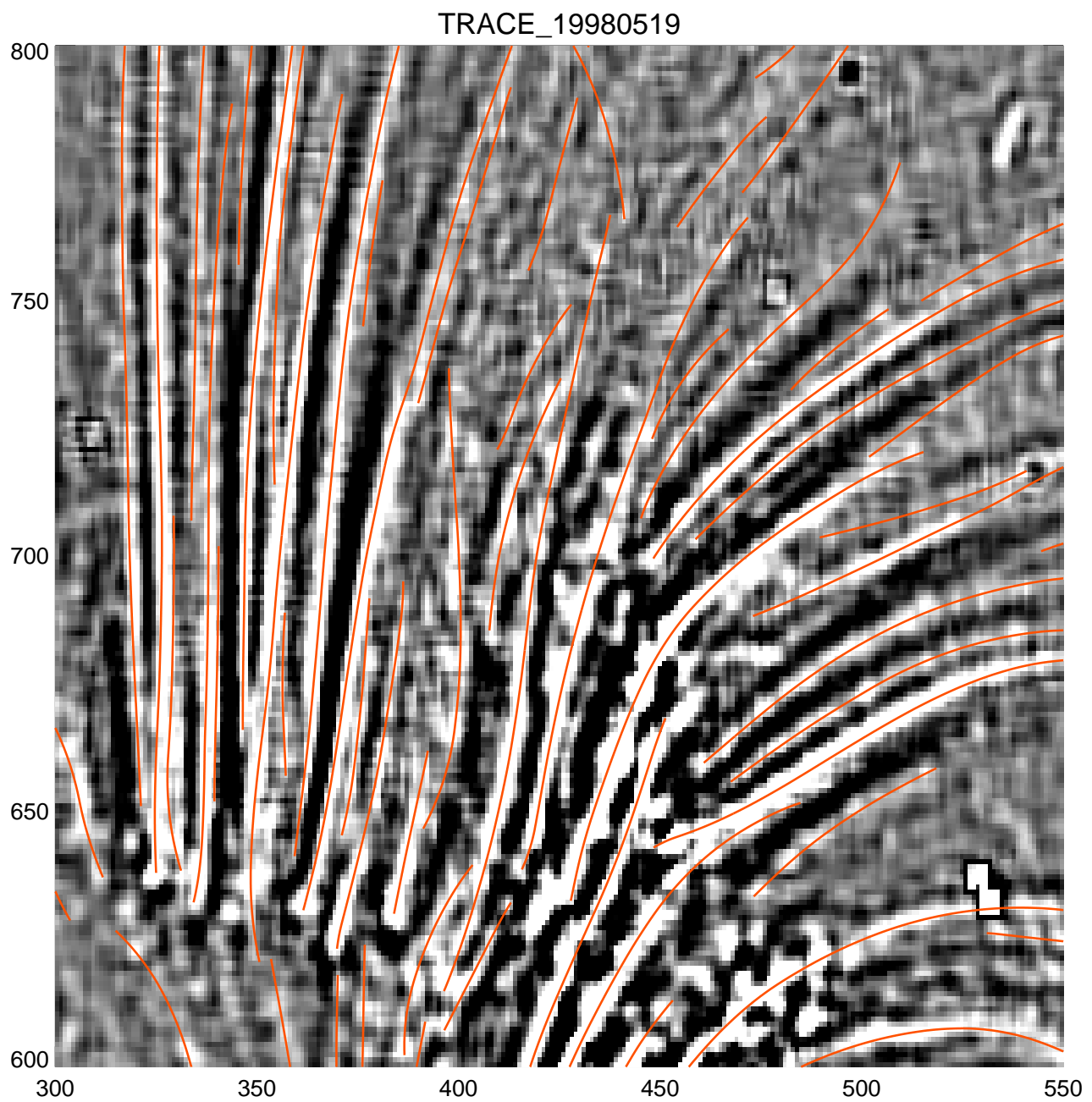


Figure 9. Example of loop tracings in area [300:550, 600:800] of the full image shown in Fig. 2. The greyscale indicates the bandpass-filtered image ($n_{sm1} = 5, n_{sm2} = 7$), and the loop tracings are shown with red curves.



359 **(8) Loop Iteration:** The steps (4) to (7) describe the tracing of a single loop, specified by the n_L
 360 coordinates $(x_i, y_i) = [x(s_k), y(s_k)]$, $k = 0, \dots, n_L - 1$. In order to proceed to the next loop we want first
 361 to erase the area of this traced loop in the residual image, so that no previously traced loop segment is
 362 traced a second time in a consecutive loop. The loop is erased in the residual image simply by setting
 363 those image pixels to zero that have a distance of $d \leq n_w = (n_{sm2}/2 - 1)$ from the loop coordinates,
 364 i.e., $z^{filter}[x_i \pm n_w, y_j \pm n_w] = 0$. An example of an image area with dense coverage of loops is shown
 365 in Fig. 9, where some loops are traced at flux levels close to the noise threshold.

366 **(9) Loop Parameters:** After we described analytically the numerical code, we summarize the free
 367 parameters and the dependent parameters (that do not require any selection by the user of the code).
 368 The code has the following free or input parameters: the lowpass filter boxcar n_{sm1} , the minimum
 369 curvature radius r_{min} , the base level factor q_{med} , in units of image median brightness values, and the
 370 corner coordinates of the noise area $[i_{n1} : i_{n2}, j_{n1} : j_{n2}]$. All other parameters are dependent, or a fixed
 371 constant, such as the tracing step $\Delta s = 1$, the highpass filter boxcar $n_{sm2} = n_{sm1} + 2$, the half width of
 372 the erased loop cross-sections $n_w = n_{sm2}/2 - 1$, and the loop termination gap $n_{gap} = 3$.

373 Acknowledgements

374 We thank Ilya Grigoriev and Anna Akhmanova for providing the images of labelled microtubules. We
 375 acknowledge also helpful discussions with Karel Schrijver, Mark DeRosa, Allen Gary, Jake Lee, Bernd
 376 Inhester, James McAteer, Peter Gallagher, Alex Young, Alex Engels, Patrick Shami, Narges Fathalian,
 377 Fatemeh Amirkhanlou, Hossein Safari, and participants of the *3rd Solar Image Processing Workshop*
 378 in Dublin, Ireland, 6 – 8 September 2006, the *4th Solar Image Processing Workshop* in Baltimore,
 379 Maryland, 26 – 30 October 2008, the *5th Solar Imaging Processing Workshop* in Les Diablerets,
 380 Switzerland, 13 – 16 September 2010, and the *6th Solar Imaging Processing Workshop* at Montana
 381 State University, Bozeman, 13 – 16 August 2012. Part of the work was supported by the NASA TRACE
 382 contract (NAS5-38099) and the NASA SDO/AIA contract NNG04EA00C.

383 References

- 384 1. Abbe, E. Note on the proper definition of the amplifying power of a lens or a lens-system, *J. Royal*
 385 *Microsc. Soc.* **1884**, 4, 348-351.
- 386 2. Aschwanden, M.J. and Nightingale, R.W. Elementary loop structures in the solar corona analyzed
 387 from TRACE triple-filter images. *Astrophys. J.* **2005**, 633, 499-517.
- 388 3. Aschwanden, M.J., Lee, J.K., Gary, G.A., Smith, M., and Inhester, B. Comparison of Five Numerical
 389 Codes for Automated Tracing of Coronal Loops. *Solar Phys.* **2008**, 248, 359-377.
- 390 4. Aschwanden, M.J. A Code for Automated Tracing of Coronal loops Approaching Visual Perception.
 391 *Solar Phys.* **2010**, 262, 399-423.
- 392 5. Aschwanden, M.J. Nonlinear Force-free Magnetic Field Fitting to Coronal Loops with and without
 393 Stereoscopy, *Astrophys. J.* **2013**, 763, 115.
- 394 6. Aschwanden, M.J. and Sun. Y. The Active Region 11158 during the 2011 February 15 X-Class Flare:
 395 Nonlinear Force-free Magnetic Fields and Free Energies Inferred from Automated Loop Tracing, (in
 396 preparation).

- 397 7. Biskri, S., Antoine, J.-P., Inhester, B., and Mekideche, F. Extraction of Solar Coronal Magnetic
398 Loops with the Directional 2D Morlet Wavelet Transform, *Solar Phys.*, **2010**, 262, 373.
- 399 8. Brangwynne, C.P., Koenderink, G.H, Barry, E., Dogic, Z., MacKintosh, F.C., and Weitz,
400 D.A. Bending dynamics of fluctuating biopolymers probed by automated high-resolution filament
401 tracking, *Biphys. J.*, **2007**, 93/(1), 346-359.
- 402 9. de Forges, H., Bouissou, A., Perez, F. Interplay between microtubule dynamics and intracellular
403 organization, *Int. J. Biochem Cell Biol.* **2012**, 44, 266-274.
- 404 10. De Pontieu, B., Erdelyi, R., and James, S.P. Solar chromospheric spicules from the leakage of
405 photospheric oscillations and flows, *Nature* **2004**, 430, 536-539.
- 406 11. De Pontieu, B., Carlsson, M., Rouppe van der Voort, L., Löfdahl, M., van Noort M., Nordlund, Å.,
407 and Scharmer, G. Rapid temporal variability of faculae: high-resolution observations and modeling,
408 *Astrophys. J.*, **2006**, 1405-1420.
- 409 12. Fuhrmann, M., Seehafer, N., Valori, G., and Wiegmann, T. A comparison of preprocessing
410 methods for solar force-free magnetic field extrapolation, *Astron. Astrophys.* **2011**, 526, A70.
- 411 13. Gary, G.A. Evaluation of a selected case of the minimum dissipative rate method for non-force-free
412 solar magnetic field extrapolation, *Solar Phys.* **2009**, 257, 271-286.
- 413 14. Gonzales, R.C., Woods, R.E.. Digital Image Processing, Pearson Prentice Hall, Upper Saddle River,
414 NJ 07458, **2008**, p.689-794.
- 415 15. Jiang, Y., Bainbridge-Smith, A., and Morris, A.B. Blood vessel tracking in retinal images, in *Proc.*
416 *of Image and Vision Computing New Zealand*, December 2007, p.126-131.
- 417 16. Kaverina, I. and Straube A. Regulation of cell migration by dynamic microtubules, *Semin. Cell*
418 *Dev. Biol.*, **2011**, 22, 968-974.
- 419 17. Koulgi, P., Sargin, M.E., Rose, K., and Manjunath, B.S. Graphical model-based tracing of curvi-
420 linear structures in bio-image sequences, in *IEEE International Conference on Pattern Recognition*,
421 **2009**, 2596-2599.
- 422 18. Lee, J.K., Newman, T.S., Gary, G.A. Automated Detection of Solar Loops by the Oriented
423 Connectivity Method. In: Proc. 17th Int. Conf. on Pattern Recognition (ICPR), Cambridge, United
424 Kingdom, **2004**, 315.
- 425 19. Lee, J.K., Newman, T.S., Gary, G.A. Oriented connectivity-based method for segmenting solar
426 loops. *Pattern Recognition* **2006**, 39, 246-259.
- 427 20. Lemen, J.R., Title, A.M., Akin, D.J., Boerner, P.F., Chou, C., Drake, J.F., Duncan, D.W., Edwards,
428 C.G., et al. The Atmospheric Imaging Assembly (AIA) on the Solar Dynamics Observatory (SDO),
429 *Solar Phys.* **2012**, 275, 17-40.
- 430 21. Martinez-Perez, M.E., Hughes, A.D., Stanton, A.V., Thom, S.A., Barath, A.A., and Parker, K.H.
431 Segmentation of retinal blood vessels based on the second directional derivative and region growing,
432 in *International Conference on Image Processing (ICIP 99*, 24-28 October 1999, 2, 173-176.
- 433 22. McAteer, R.T.J., Gallagher, P.T., and Ireland, J. Statistics of Active Region Complexity: A Large-
434 Scale Fractal Dimension Survey, *Astrophys. J.* **2005**, 631, 628-635.
- 435 23. Metcalf, T.R., Jiao, L., Uitenbroek, H., McClymont, A.N., and Canfield, R.C. Is the solar
436 chromospheric magnetic field force-free? *Astrophys. J.* **1995**, 439, 474-481.

- 437 24. Pawley, J.B. and Masters B.R. Handbook of Biological Confocal Microscopy, *J. Biomedical Optics*
438 **2008**, 13/2, p. 029902.
- 439 25. Sargin, M.E., Altinok, A., Rose, K., and Manjunath, B.S. Tracing curvi-linear structures in live cell
440 images, in *IEEE International Conference on Image Processing (ICIP 07)*, 16-19 September 2007, 6,
441 285-288.
- 442 26. Subramaniam, R., Kapoor, T.M. Building complexity: insights into self-organized assembly of
443 microtubule-based architectures, *Dev. Cell* **2012**, 22, 874-885.
- 444 27. Tang, J. and Acton, S.T. Vessel boundary tracking for intravital microscopy via multiscale gradient
445 vector flow snakes, in *IEEE International Conference on Acoustics, Speech, and Signal Processing*
446 (*ICASSP 04*, 17-21 May 2004, 51, no. 2, 316-324.
- 447 28. Tsien, R.Y. The green fluorescent protein, *Annu. Rev. Biochem.* **1998**, 67, 506-544.
- 448 29. Wade, R.H., Chrétien, D. Cryoelectron microscopy of microtubules. *J. Struct. Biol.* **1993**, 110,
449 1-27.
- 450 30. Xiong, G., Zhou, X., Degterev, A., Ji, L., and Wong, S.T. Automated neurite labeling and analysis
451 in fluorescence microscopy images, *Cytometry Part A* **2006** 69A, no. 6, 494-505.
- 452 31. Zhang, Y., Zhou, X., Witt, R.M., Sabatini, B.L., Adjero, D. and Wong, S.T. Dendritic spine
453 detection using curvi-linear structure detector and Ida classifier, *NeuroImage* **2007** 36, no. 2,
454 346-360.

455 © November 10, 2021 by the authors; submitted to *Entropy* for possible open access
456 publication under the terms and conditions of the Creative Commons Attribution license
457 <http://creativecommons.org/licenses/by/3.0/>.